

UCLA/12/TEP/00

Dark Matter Search Using *XMM-Newton* Observations of Willman 1

Michael Loewenstein^{1,2,3}, and Alexander Kusenko^{4,5}

ABSTRACT

We report the results of a search for an emission line from radiatively decaying dark matter in the ultra-faint dwarf spheroidal galaxy Willman 1 based on analysis of spectra extracted from *XMM-Newton* X-ray Observatory data. The observation follows up our analysis of *Chandra* data of Willman 1 (Loewenstein & Kusenko 2010) that resulted in line flux upper limits over the *Chandra* bandpass and evidence of a 2.5 keV feature at a significance below the 99% confidence threshold used to define the limits. The higher effective area of the *XMM-Newton* detectors, combined with application of recently developing methods for extended-source analysis, allow us to derive improved constraints on the combination of mass and mixing angle of the sterile neutrino dark matter candidate. We do not confirm the *Chandra* evidence for a 2.5 keV emission line.

1. Introduction

Sterile neutrinos represent a plausible dark matter candidate amenable to observation via X-ray spectroscopy of locations in the universe where the dark matter surface density is high. Sterile neutrinos, gauge-singlet fermions that emerge in extensions of the Standard Model of particle physics that explain ordinary neutrino masses, may comprise some or all

¹Department of Astronomy, University of Maryland, College Park, MD.

²Center for Research and Exploration in Space Science and Technology

³X-ray Astrophysics Laboratory, Mail Code 662, NASA Goddard Space Flight Center, Greenbelt, MD 20771, USA

⁴Department of Physics and Astronomy, University of California, Los Angeles, CA 90095-1547, USA

⁵Institute for the Physics and Mathematics of the Universe, University of Tokyo, Kashiwa, Chiba 277-8568, Japan

of the dark matter if the Majorana masses are below the electroweak scale (Kusenko 2009). If their mass lies in the 1–30 keV range, non-resonant oscillations produce sterile neutrinos at an abundance comparable to that inferred for dark matter (Dodelson & Widrow 1994) – although several other production channels have been suggested (Kusenko 2009). Sterile neutrinos in this mass range may explain the observed velocities of pulsars by anisotropic emission of sterile neutrinos from a cooling neutron star born in a supernova explosion (Kusenko & Segrè 1997; Fuller et al. 2003) and can facilitate early star formation (Kusenko 2009). As a form of warm dark matter (WDM), sterile neutrinos (Abazajian et al. 2001; Petraki 2008; Boyanovsky 2008; Boyanovsky & Wu 2011; Dunstan et al. 2011) may resolve some of the discrepancies (Ferrero et al. 2011, and references therein) between Cold Dark Matter (CDM) models (Lovell et al. 2011; Menci, Fiore, & Lamastra 2012) and the observed structure in the universe. A number of particle physics models have been proposed to accommodate a sterile neutrino with the requisite mass and mixing, including ν MSM (Asaka & Shaposhnikov 2005; Boyarsky, Ruchayskiy, & Shaposhnikov 2009), split seesaw (Kusenko, Takahashi, & Yanagida 2010), Higgs singlet (Kusenko 2006; Petraki & Kusenko 2008), and other models. For example, the split seesaw mechanism (Kusenko, Takahashi, & Yanagida 2010) with one extra dimension causes the mass and mixing of a sterile neutrino originating at a high scale to be exponentially suppressed in the low-energy effective theory, which makes it a good dark matter candidate, while preserving both the standard seesaw explanation for the neutrino masses and the explanation of the matter-antimatter asymmetry of the universe by leptogenesis (Fukugita & Yanagida 1986).

The one-loop decay of relic keV sterile neutrinos into an active neutrino and photon with energy $E_\gamma = m_{\text{st}}c^2/2$ produces an X-ray emission line with width corresponding to the velocity dispersion of the dark matter distribution within the observed solid angle. While the prospects of discovering a dark-matter sterile neutrino in a laboratory present a daunting challenge (Ando & Kusenko 2010; Bezrukov & Shaposhnikov 2007), the narrow decay line allows one to search for relic sterile neutrinos using X-ray telescopes (Abazajian et al. 2001). The high dark matter concentrations of dwarf spheroidal galaxies make them prime targets for dark matter searches, with the additional advantage of the total absence of competing intrinsic X-ray sources. Moreover, as the most dark matter dominated objects known they are not subject to systematic uncertainties that derive from decomposing the mass into baryonic and non-baryonic components – although assumptions about membership and dynamical equilibrium come into play in converting measured velocity dispersion profiles into dark matter mass estimates. We initiated a dedicated search for sterile neutrinos with the *Suzaku* X-ray telescope, placing new limits on sterile neutrinos over the 1–20 keV mass range from XIS spectra of the Ursa Minor dwarf spheroidal galaxy (Loewenstein, Kusenko, & Biermann 2009).

We continued the search with *Chandra* observation of the ultra-faint dwarf spheroidal Willman 1 (Loewenstein & Kusenko 2010, ApJ, 700, 426; hereafter LK10), considered at the time to be a particularly compelling target for dark matter searches (though its status subsequently changed somewhat; see below). 99% confidence line flux upper limits over the 0.4-7 keV *Chandra* bandpass were derived and mapped to an allowed region in the sterile neutrino mass-mixing angle plane consistent with the *Suzaku* constraints. In addition we reported evidence for an emission line with flux below this threshold from radiative decay of a 5 keV sterile neutrino with a mixing angle in the narrow range where oscillations produce all of the dark matter and for which sterile neutrino emission from the cooling neutron stars can explain pulsar kicks (LK10). This tentative result is best confirmed (or refuted) by utilizing the large effective area of the *XMM-Newton* EPIC detectors; and, we were awarded observing time on Willman 1 for this purpose. Here we present results of our analysis of these data, deriving more stringent constraints on sterile neutrino parameters and failing to confirm the best-fit estimate of the *Chandra* 2.5 keV line flux.

2. Data Analysis

2.1. Observation and Data Processing

Willman 1 was observed with *XMM-Newton* in three segments in late October 2010: ObsID 0652810101 (for 29356 s on 10/22), ObsID 0652810301 (36054 on 10/25), and ObsID 0652810401 (36218 s on 10/31). In addition, a region offset by 1 degree was observed (ObsID 0652810201; 33856 s on 10/30). The last was primarily meant as a control in the event of a positive emission line detection; and, as none was found we will not consider these data further (although they were reduced and analyzed in parallel to the on-source data). We utilize data from the two EPIC-MOS (hereafter, EMOS = EMOS1 + EMOS2), as well as the EPIC-PN (hereafter, EPN), CCD detectors. Data reduction, background modeling, and spectral extraction are conducted with the *XMM-Newton* Extended Source Analysis Software (XMM-ESAS) – part of the XMM-Newton Science Analysis System (SAS v11.1 is used throughout) – and methods as detailed in Kuntz & Snowden (2008) and Snowden et al. (2008). A summary of our particular application of these techniques follows; further details on the approach and individual procedures and may be found in the XMM-ESAS “cookbook”¹.

In order to apply the latest calibration files and products, rather than use pipeline-

¹<http://heasarc.gsfc.nasa.gov/docs/xmm/xmmhp.xmmesas.html>

processed data, the unprocessed event files are reduced to create filtered event files using the composite tools *emchain* and *mos-filter* (*epchain* and *pn-filter*) for EMOS (EPN) datasets. This results in the removal of time intervals of prominent soft proton (SP) flaring – identified by hard (2.5–12 keV) energy band background count rates deviating by more than 1.5σ from the mean of a Gaussian distribution that characterizes the count rate histogram. Out-of-time (OOT) EPN events that correspond to photons registered during CCD readout are processed in parallel to ordinary EPN events for subsequent correction (see below). Exposure times for the final cleaned event files are shown in Table 1. Primarily due to flaring, data from \sim one-third of the EMOS, and $\sim 60\%$ of the EPN, exposures are excluded in the end.

2.2. The Extraction of Source and Background Spectra

We exclude background point source as follows. Source detection is conducted with the SAS v11 composite *edetect_chain* tool as a standalone procedure and as incorporated in the XMM-ESAS *cheese* procedure. These are used in the construction of region masks in detector coordinates for use in spectral extraction. We considered masks that (a) minimize the excluded regions by restricting only the cores (the inner $8''$ in radius) of the brightest sources (those with $\text{likelihood} > 40$), (b) that minimize contamination from point sources ($32''$ radii for sources detected with $\text{likelihood} > 10$), as well as (c) an intermediate choice ($16''$ radii for sources detected with $\text{likelihood} > 10$). We also considered three spectral extraction regions. The first corresponds to $1.7\times$ the half-light radius ($1.7 \times 25 \text{ pc} \equiv 232''$ at the 38 kpc Willman 1 distance) within which the mass is particularly well-determined (Amorisco & Evans 2011) and for which we apply mask “a” above, the second to 150 pc ($818''$; mask “b”), and the third to 100 pc ($545''$; mask “c”) – the mass distribution is estimated within 100 pc in Strigari et al. (2008).

Files were processed with *FLAG* == 0 and screened to retain only those events with *PATTERN* ≤ 12 (four-or-fewer pixel events) for EMOS, and *PATTERN* ≤ 4 (single and double pixel events) for EPN, spectra as a means to exclude non-X-ray events. The

Table 1. Final Good Time Intervals in ks

| ObsId | EMOS1 | EMOS2 | EPN |
|------------|-------|-------|-------|
| 0652810101 | 15.37 | 19.21 | 9.53 |
| 301 | 21.86 | 23.13 | 15.47 |
| 401 | 27.30 | 28.43 | 16.16 |
| total | 64.53 | 70.70 | 41.16 |

XMM-ESAS *mos-spectra* and *mos-back* (*pn-spectra* and *pn-back*) procedures are used to extract EMOS (EPN) source and quiescent particle background (QPB) spectra, and to compute spectral response files. This method utilizes filterwheel-closed data, data from the unexposed corners of archived *XMM-Newton* observations, and ROSAT All-Sky Survey (RASS) data to produce a model QPB spectrum. Chips found to be in anomalous states with elevated low-energy background according to the XMM-ESAS criteria (EMOS1-ccd4 and -ccd5 for ObsID 0652810301 and ObsID 0652810401, EMOS2-ccd5 for ObsID 0652810101) are excluded, and EMOS-1ccd6 was no longer operating at the time of these observations. The detector extraction areas are calculated using the *proton_scale* task. The spectral extraction procedure generates instrument response matrices in the form of separate redistribution matrix (**rmf**) and effective area function (**arf**) files.

2.3. Spectral Analysis

2.3.1. The Baseline Spectral Model

The XMM-ESAS procedures create model QPB background spectra appropriate to the conditions during the observation under consideration; however, a number of internal and astrophysical background components remain that must be included in any spectral model. This approach is both more accurate and more conservative than one where blank-sky background is subtracted, given the directional dependence of the intensity and spectral shape of the cosmic contribution, and the time dependence of the particle and instrumental backgrounds. Moreover, in the event that there is dark matter line emission the “blank-sky” includes a contribution to the signal that ought not be subtracted.

The instrumental background includes a number of fluorescent lines. The strongest of these – the 1.49 keV Al $K\alpha$ (EMOS and EPN) and 1.75 keV Si $K\alpha$ (EMOS only) features are sufficiently variable that the XMM-ESAS model QPB spectrum includes a smooth bridge over the relevant spectral region, and the lines must be included in spectral modeling in the form of narrow Gaussians. Other problematic EPN lines are avoided by restricting the bandpass to < 7 keV.

Even after filtering, contamination from residual SP flaring and solar wind charge exchange (SWCX) are commonly present. These are modeled using a broken power-law and a pair of unresolved emission lines at 0.56 keV (OVII) and 0.65 keV (OVIII) that dominate SWCX spectra, respectively. Since energy from the SP component is directly deposited in the detectors, diagonal response files are used for this component in place of the telescope responses described above.

The astrophysical X-ray background includes multiple components that we model with thermal plasma (**apec**) models to account for the emission from the Local Hot Bubble (LHB) and the Milky Way Halo (MWH), and a power-law for the unresolved point sources mostly originating from background AGN (CXB). The elemental composition in the **apec** components are set at their solar abundances as defined in Asplund et al. (2009). We use the HEASARC background tool² to extract the ROSAT All-Sky Survey (RASS) spectrum from a 1° radius aperture centered on the position of Willman 1 for use in constraining the parameters of these components.

2.3.2. Fitting Techniques and Best-Fit Baseline Models

Spectra are fitted using XSPEC version 12.7³. The final total spectral model we adopt may be expressed, in XSPEC notation, as **bknpower** + **gaussian** + **gaussian** + **constant** × **constant** × (**gaussian** + **gaussian** + **apec** + (**gaussian** + **apec** + **apec** + **constant** × **powerlaw**) × **TBabs**), where **bknpower** represents the residual SP component (with its distinct diagonal response matrix), the first pair of **gaussians** the Al $K\alpha$ and Si $K\alpha$ instrumental lines, and the second pair of **gaussians** the SWCX emission. The remaining astrophysical background consists of the unabsorbed **apec** LHB and absorbed (two-temperature) **apec** + **apec** MWH, as well as the absorbed **powerlaw** CXB emission. The **constant** factor multiplying the CXB represents the departure of the CXB intensity from its all-sky average (Kushino et al. 2002) due to cosmic variance and the fact that the resolved portion of the CXB is removed. The Tuebingen-Boulder ISM absorption model (Wilms, Allen, & McCray 2000), **tbabs**, is applied with the column density fixed at the Galactic value of $1.13 \times 10^{20} \text{ cm}^{-2}$ (Dickey & Lockman 1990). The two multipliers that act on all of the sky components, **constant** × **constant**, represent the size of the spectral extraction region (see above) so that all normalizations correspond to fluxes per solid angle, and a factor to account for any detector calibration offset.

There are datasets from three detectors for each of the three on-source ObsIDs. We initially analyze each dataset separately. As is usually the case, we find that the EMOS1 and EMOS2 spectra are very similar for each observation, and we always analyze these in tandem with all LHB, MWH, and CXB component parameters tied together. Due to systematic differences between the EMOS and EPN CCDs, particularly with regard to details in particle background for extended sources, we always fit these data separately and derive

²<http://heasarc.gsfc.nasa.gov/cgi-bin/Tools/xraybg/xraybg.pl>

³<http://heasarc.gsfc.nasa.gov/docs/xanadu/xspec/>

independent constraints on sterile neutrino line emission from each set of detectors. Joint fits would invite the introduction of a bias in the best fit model parameters and could lead to the underestimation of errors by artificially degrading the model goodness-of-fit (e.g., Baldi et al. 2012).

Although the corresponding systematics are less severe we choose not to coadd the datasets from the three separate observation intervals, fitting them first separately and then simultaneously as we shortly describe in detail. Our final results are taken from the latter. All parameters are tested to see if they are well-determined, if fits are sensitive to their values, and if limits on additional line emission over a range of representative energies are significantly affected by their variation. When thus justified, these are fixed as described below. The following is based on extensive experimentation, from which models with a minimum number of significant, variable parameters emerge that lead to a robust limit on sterile neutrino line emission.

In the simultaneous fits, the Al $K\alpha$ and Si $K\alpha$ energies and widths are fixed at the values determined from the individual observation fits. The SWCX line energies are fixed at 0.56 and 0.65 keV, and their widths at 1 eV (negligible compared to the EPIC resolution). The LHB temperature is fixed at 0.15 keV, the MWH temperatures at 0.10 and 0.34 keV based on fits that included the RASS spectrum, and the CXB slope at 1.46 (Kushino et al. 2002). The EMOS1/EMOS2 offset is set to unity.

In what follows, we restrict discussion to the 100 pc radius circular aperture spectral extraction region. The increase in counts provided superior statistical accuracy to the 42.5 pc ($1.7\times$ the half-light radius) region. Given the systematic mass uncertainties (see below), we judge that this compensates for the formally smaller uncertainty in the mass enclosed within the smaller aperture. While the larger extraction aperture for the 150 pc region encompasses a larger flux, the effect of vignetting increases the ratio of non-X-ray to X-ray events and degrades the statistical accuracy.

We first consider the unbinned, unsubtracted⁴ spectra over the “global” 0.3–10 (0.4–4) keV energy range for the EMOS (EPN), fit by minimizing the modification of the C-statistic (Cash 1979) implemented in XSPEC as *cstat* (we refer to this approach as “*cstat-nbs*”, where nbs refers to “no background subtraction”). Since the CXB is much smaller than the QPB, its normalization (relative to the all-sky average; see above) is also fixed at values determined from the separate observation fits. The SWCX norms are set to 0, and the relative observation-to-observation offsets are set to 1. Thus the free parameters are the separate SP

⁴Here, “background-subtracted” and “unsubtracted” always refers to whether or not the QPB – only – is subtracted prior to fitting.

broken power-law slopes for each detector and each observation, and the SP broken power-law energy break for each detector (linked at an identical value across observations). The free normalizations include those for the SP component and instrumental lines for each detector and each observation, and those for the LHB and MWH (tied for each set of EMOS or EPN detectors for each observation).

The following minor statistical issue arises with respect to the EPN regarding out-of-time (OOT) events. The XMM-ESAS *pn-back* task produces an OOT-subtracted spectrum that is not purely Poissonian, and the *cstat* statistic that we sometimes employ is strictly valid only for data with Poisson errors. We address this by including an explicit OOT background in these cases, scaling the OOT spectra created by the XMM-ESAS *pn-spectra* task by 0.063 (Nevalainen, Markevitch, & Lumb 2005). Results using the presubtracted spectra are consistent, as expected given the small departure from Poissonian, with the approach we adopt – although the latter yields somewhat better fits.

Although these are not utilized to derive best-fits or sterile neutrino line flux constraints, for purposes of illustrating the relative strengths of the spectral model components and the overall signal-to-noise of the data we show the coadded EMOS (EMOS1 and EMOS2, all observations) and EPN (all observations) total spectra and mean best-fitting model in Figure 1.

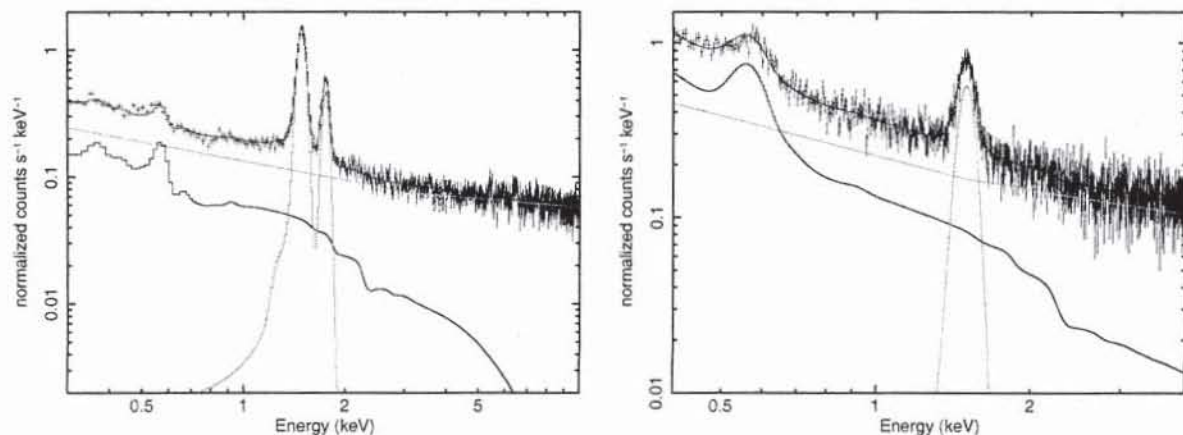


Fig. 1.— The *left* panel (a) (*right* panel (b)) shows the total co-added EMOS (EPN) unsubtracted spectrum (black errorbars), and mean best-fitting model (red curve) composed of astrophysical (sum of LHB, MWH, and CXB; blue curve) background, particle background (SP; green broken power-law), and instrumental fluorescent lines (orange). This is meant to illustrate overall S/N and the spectral decomposition; co-added spectra are not used to derive spectral analysis results.

Because of the prominence of the (unsubtracted) instrumental fluorescent lines, deriving limits on additional line emission is highly problematic in the 1.2-1.9 (1.3-1.65) keV energy

range based on EMOS (EPN) spectra. As a result it is sensible to split the spectrum into low- and high-energy segments on either side, and treat these separately. Moreover, since some of the model components are negligible in one or the other of these segments one can apply simpler models with parameters that are a subset of those in the global fit. Ultimately, the constraints on sterile neutrino line emission are derived from fits to these low- and high-energy sub-spectra, with the role of global fits purely to provide a means of setting these up.

We proceed with the analysis described above in the low energy spectral segments (0.3–1.2 keV for the EMOS, 0.4–1.3 keV for the EPN) by freezing the instrumental line norms at the values derived from the global fits, reactivating the SWCX lines (with normalizations tied across observations), and with the SP component model converted to a single-slope power-law allowed to vary from observation to observation. We follow with fitting of the high energy (1.9–10 keV for the EMOS, 1.65–4 keV for the EPN) spectral segments by freezing the LHB, MWH, and SWCX normalizations and converting the SP component back to a broken power law for the EMOS; parameters (slopes, break energies if applicable) are tied across observations. Spectra and best-fit models are shown in Figure 2.

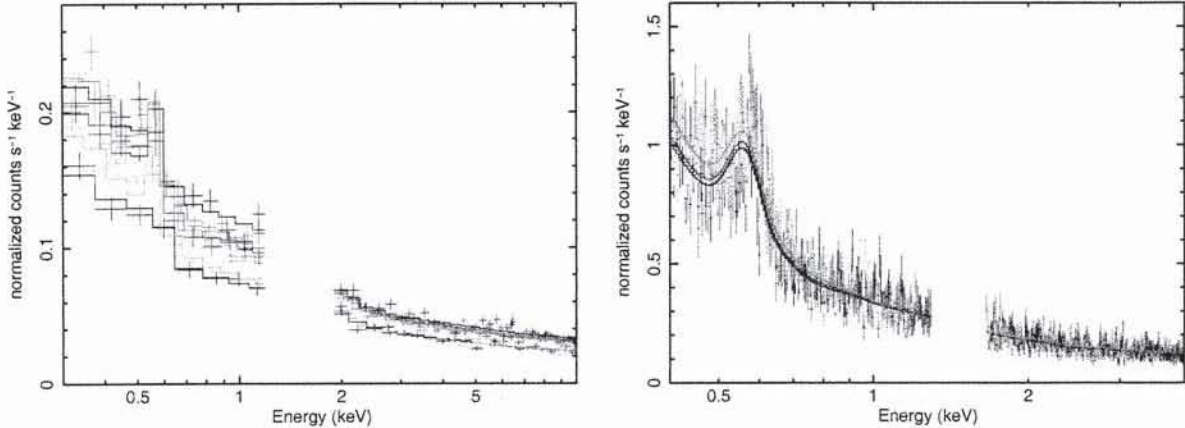


Fig. 2.— The *left* panel (a) (*right* panel (b)) shows the 6 (3) individual EMOS (EPN) spectra (with some binning) and best-fit models for the simultaneous *cstat* fits to the unsubtracted spectra. Low- and high-energy segments, although shown together here, are separately fitted (see text for details).

In our second approach we consider (QPB) background-subtracted, binned (minimum 15 counts per bin) spectra fit by minimizing the χ^2 statistic (we refer to this approach as “ χ^2 -bs”). The global EPN bandpass may now be extended to 7 keV (residual instrumental features at ~ 4.5 and ~ 5.5 keV that preventing this in the unsubtracted spectrum are now subtracted out). With the increased prominence of the CXB relative to the SP, we now fix the SP parameters (though not their normalizations) to the best-fit values determined above, and thaw the CXB norm (relative to its all-sky value) which is tied across observations.

For the low-energy sub-spectra, the instrumental line normalizations are again fixed at the values derived from the global fits and the SWCX lines are reactivated. In addition, the CXB normalization is now fixed. In following this with fitting of the high energy sub-spectra the LHB, MWH, and SWCX normalizations are frozen, but the CXB normalization thawed and allowed to separately vary for each observation. Again, for illustrative purposes, the coadded subtracted spectra and corresponding mean best-fitting model are shown in Figure 3. Spectra and best-fit models for the individual spectra in each of the two energy intervals are shown in Figure 4.

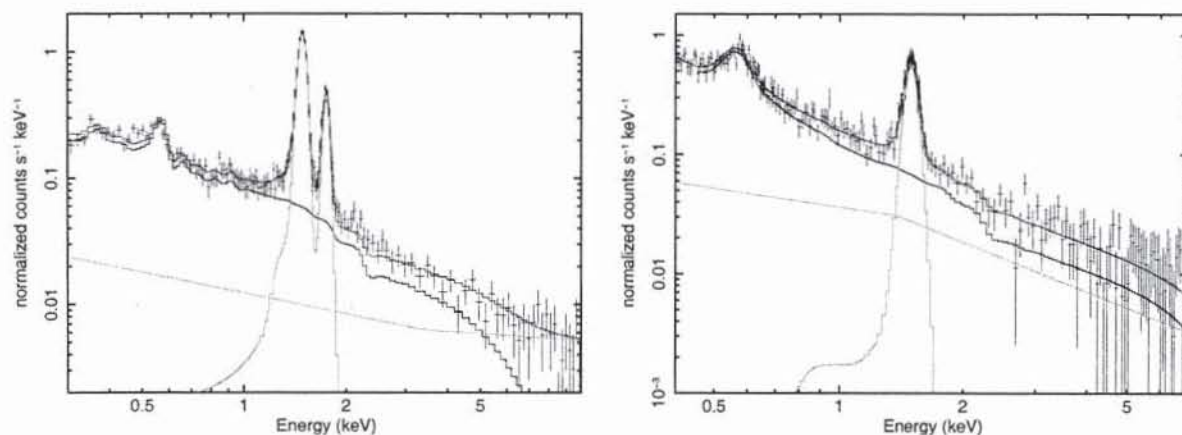


Fig. 3.— Same as Figure 1 for the subtracted spectra (with some binning).

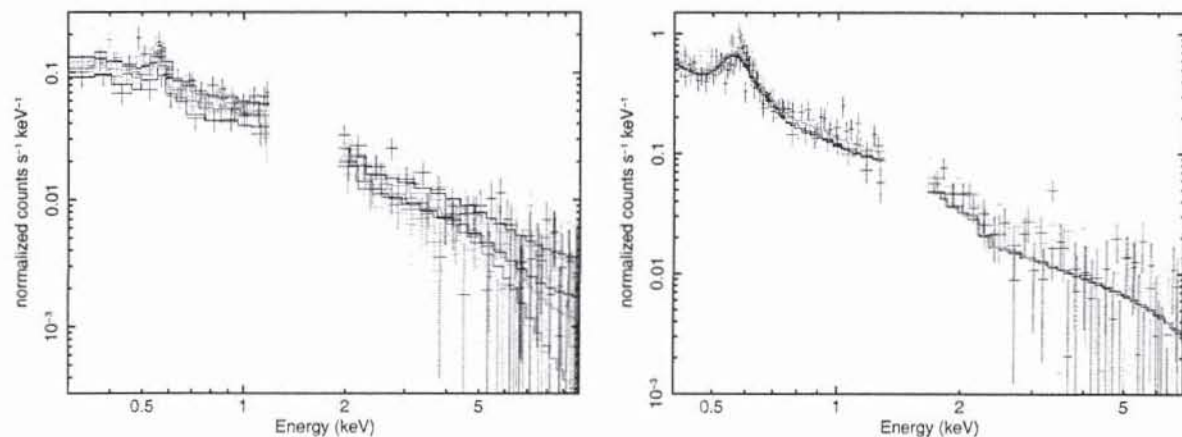


Fig. 4.— Same as Figure 2 for the subtracted spectra (with some binning, and on a logarithmic scale).

Finally, we also consider joint fitting of the total (unsubtracted) and background (QPB) spectrum. Here the background spectrum, which is not Poissonian, is binned to a minimum of 50 counts per bin and fitted by application of χ^2 statistics, while the total spectrum is unbinned and fit by applying the *cstat* statistic. Thus, the best-fit model parameters are

determined from minimization of a hybrid statistic. The global fits proceed as in the first approach with SP and instrumental parameters and normalizations tied in the models for the total and QPB spectra, and the other (SWCX, LHB, MWH, and CXB) component normalizations set to zero in the latter (thus no additional parameters are introduced). For the low-energy sub-spectrum, the SP is characterized by a broken power-law fixed across observations and detectors. This is also the case for the high-energy EMOS spectrum, while the SP is assumed to be a single-slope power-law for the high-energy spectral EPN segment.

The fit statistics for all three approaches are displayed in Table 2, along with the 90% ($\Delta - statistic = 2.71$, where “statistic” refers to the fit statistic – either χ^2 , the modified C-statistic, or the hybrid statistic described above) confidence upper limits on the surface brightness of a narrow emission line with energy fixed at 2.5 keV. Negative emission line fluxes are permitted when deriving these limits.

2.4. Emission Line Flux Limits at 2.5 keV and Other Energies

Having established the baseline models as described above, we derive upper limits as in Loewenstein et al. (2009), and LK10. An unresolved Gaussian component, stepped in 10 eV intervals over the relevant bandpass, is added to the baseline model, and $\Delta - statistic = 9.21$ (99%) upper confidence levels on the line flux (that is permitted to be negative) are computed. Limits for the low- and high-energy segments are separately computed with the spectral model parameters fixed or variable as described above – except for the SWCX component that we always fix at their best-fit values (with the – necessary – inclusion of this component in *XMM-Newton* spectra, limits obtained in the ~ 0.55 -0.66 keV region using this method are provisional). The limits, in 150 eV bins for the χ^2 -bs and *cstat-nbs* approaches applied both to the EMOS and EPN detectors, with zooms on the higher-energies for the latter, are shown in Figure 5. Given the similarity of the limits from the two approaches we henceforth adopt the χ^2 -bs limits. The χ^2 -bs constraints are formally more restrictive for the EPN detector in the 4-7 keV bandpass. However as this is a result of an overall shift in the allowed line flux and not of an improvement in accuracy and, given the residual background artifacts in this energy range (§2.3.2), we also restrict our subsequent discussion to constraints derived from the EMOS detectors.

The expected line flux from sterile neutrino radiative decay in Willman 1, produced by active-sterile neutrino transitions with standard assumptions about the lepton asymmetry and thermal history of the universe below ~ 1 GeV (LK10 and references therein; also, see below), is shown by the solid lines in Figures 5ab (the star in (c) shows the prediction for $m_{st} = 2.5$ keV). The broken line shows the allowed range taking the impact of hadronic

Table 2. Fit Statistics – 100 pc Extraction Region

| method | bandpass | detector | stat | best-fit-stat | $\Sigma_X(2.5)$ |
|------------------|----------|----------|--------------|---------------|-------------------------|
| <i>cstat-nbs</i> | global | EMOS | <i>cstat</i> | 3993/3841 | ... |
| | | EPN | | 2108/2153 | ... |
| | lo-en | EMOS | | 340/337 | ... |
| | | EPN | | 492/532 | ... |
| | hi-en | EMOS | | 3342/3225 | $-0.34^{+0.99}_{-1.03}$ |
| | | EPN | | 1416/1403 | $1.14^{+1.51}_{-1.46}$ |
| χ^2 -bs | global | EMOS | χ^2 | 1545/2488 | ... |
| | | EPN | | 2032/2025 | ... |
| | lo-en | EMOS | | 221/341 | ... |
| | | EPN | | 499/500 | ... |
| | hi-en | EMOS | | 1021/1866 | $0.70^{+1.26}_{-1.23}$ |
| | | EPN | | 1354/1328 | $1.73^{+1.48}_{-1.41}$ |
| hybrid | global | EMOS | <i>hstat</i> | 4359/4535 | ... |
| | | EPN | | 2812/2505 | ... |
| | lo-en | EMOS | | 390/442 | ... |
| | | EPN | | 654/681 | ... |
| | hi-en | EMOS | | 3630/3819 | $0.39^{+0.80}_{-0.76}$ |
| | | EPN | | 1732/1608 | $2.73^{+1.46}_{-1.10}$ |

Note. — Shown are the fit statistics (per degree-of-freedom) for the best-fit model determined using the three analysis approaches – unbinned, background-unsubtracted source spectral fitting with the (modified) C-statistic (“*cstat-nbs*”), binned, background-subtracted source spectral fitting with the χ^2 statistic (“ χ^2 -bs”), joint unsubtracted-source/background spectral fitting using a combination of the χ^2 and C-statistic (“hybrid”) – see text for details. Also shown are the best-fit and 90% confidence limits on the average surface brightness in units of 10^{-8} photons $\text{cm}^{-2} \text{s}^{-1} \text{arcmin}^{-2}$, of a narrow emission line with energy fixed at 2.5 keV.

uncertainties, which affect the relation between the mass and the mixing angle, into account (Asaka, Laine, & Shaposhnikov 2007). An average total (sterile neutrino) dark matter surface density of $200 \text{ M}_\odot \text{ pc}^{-2}$ is adopted (see below). A sterile neutrino produced in this way in sufficient abundance to compose all of the dark matter produces an emission line that exceeds the observed limits if $m_{\text{st}} > 5 \text{ keV}$. That is, the presence of a 2.5 keV line corresponding to the parameters of the best-fit *Chandra* estimate is not confirmed. We further illustrate this in Figure 6 that compares, for both approaches and for the EPN and EMOS, measured spectra and best-fit models that include a narrow 2.5 keV emission line with strength fixed at that predicted for radiative decay of sterile neutrinos produced by non-resonant oscillations. There is no evidence of such a feature in the *XMM-Newton* spectra.

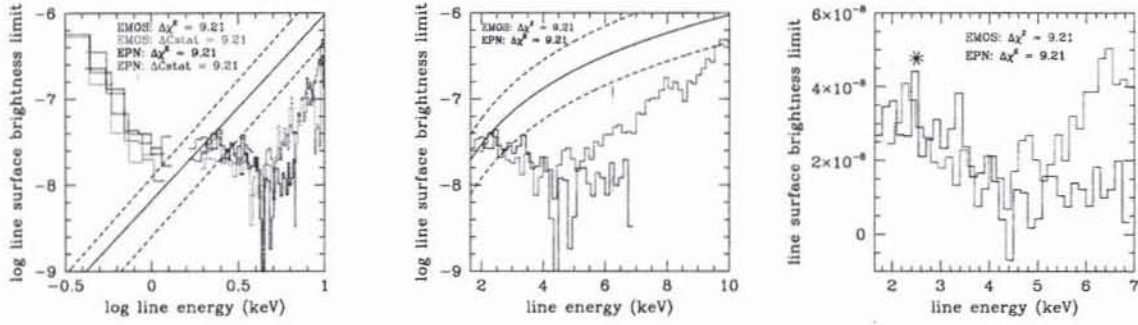


Fig. 5.— Upper limits on the emission line surface brightness, in units of photons $\text{cm}^{-2} \text{ s}^{-1} \text{ arcmin}^{-2}$ and averaged over the inner 100 pc of Willman 1, for both EMOS and EPN detectors and χ^2 -bs and *cstat*-nbs approaches as indicated in the embedded legend (*left panel* (a)), with focus on the high-energy spectra segment (χ^2 -bs approach) in *middle* (b) and *right* (c) panels. The solid and broken lines show the expected line flux from sterile neutrino radiative decay in Willman 1, for an average total (sterile neutrino) dark matter surface density of $200 \text{ M}_\odot \text{ pc}^{-2}$ (see text), taking into account the hadronic uncertainties in production (Asaka et al. 2007). The star in (c) shows the mean prediction for $m_{\text{st}} = 2.5 \text{ keV}$.

3. Limits on Sterile Neutrino Parameters from the *XMM-Newton* Spectrum of Willman 1

The equations relating the dark matter projected surface mass density Σ_{dm} , X-ray observables (line energy E_γ , and line surface brightness Σ_{line}), and sterile neutrino parameters (mass m_{st} , mixing angle θ , and fraction of dark matter in sterile neutrinos f_{st}), are the following (see, e.g., LK10 and references therein):

$$m_{\text{st}} = 2E_\gamma, \quad (1)$$

$$\Gamma_{\nu_s \rightarrow \gamma \nu_a} = 5.52 \times 10^{-32} \left(\frac{\sin^2 \theta}{10^{-10}} \right) \left(\frac{m_{\text{st}}}{\text{keV}} \right)^5 \text{ s}^{-1}, \quad (2)$$

and

$$\Sigma_{\text{line}} = 3.95 \times 10^{17} \Gamma_{\nu_s \rightarrow \gamma \nu_a} f_{\text{st}} \left(\frac{\Sigma_{\text{dm}}}{\text{M}_{\odot} \text{ pc}^{-2}} \right) \left(\frac{E_{\gamma}}{\text{keV}} \right)^{-1} \text{ photons cm}^{-2} \text{ s}^{-1} \text{ arcmin}^{-2}, \quad (3)$$

where the expression for the decay rate of relic keV sterile neutrinos into an active neutrino and photon, $\Gamma_{\nu_s \rightarrow \gamma \nu_a}$, is given for Majorana sterile neutrinos.

As in LK10 we estimate the average dark matter surface mass density within 100 pc based on projecting the best-fit NFW (Navarro, Frenk, & White 1997) mass model in Strigari et al. (2008); however, we now introduce a (tidal) truncation radius of 930 pc (Sánchez-Conde et al. 2011) by adopting the “ $n = 2$ BMO” generalization of the NFW profile (Oguri & Hamana 2011). This yields $135 \text{ M}_{\odot} \text{ pc}^{-2}$ from the dark matter in Willman 1, to which we (conservatively) add $65 \text{ M}_{\odot} \text{ pc}^{-2}$ (LK10) associated with dark matter in the Milky Way halo to obtain a fiducial total line-of-sight surface mass density $\Sigma_{\text{dm}}(100 \text{ pc}) = 200 \text{ M}_{\odot} \text{ pc}^{-2}$. The resulting mass profile is consistent with other estimates (Wolf et al. 2009; Amorisco & Evans 2011). However $\Sigma_{\text{dm}}(100 \text{ pc})$ is uncertain by a factor of 2 or more, considering the errors associated with those in the velocity dispersion profile, as well as the dynamical state of Willman 1 (see discussion below).

The upper limit on the dark matter radiative decay rate as a function of energy from equation (3) with $f_{\text{st}} = 1$ is shown in Figure 7, where we also show the limits for $\Sigma_{\text{dm}}(100 \text{ pc}) = 100 \text{ M}_{\odot} \text{ pc}^{-2}$ (or, equivalently, $f_{\text{st}} = 0.5$). As in LK10 and Loewenstein et al. (2009) we map this into excluded regions in the m_{st} - θ sterile neutrino parameter space under each of the following two separate assumptions: (1) that all of the dark matter is composed of sterile neutrinos produced by some unspecified mechanism, (2) that non-resonant oscillations, as first suggested by Dodelson & Widrow (1994), produced sterile neutrinos at the abundance determined by m_{st} and θ as calculated in Asaka et al. (2007) (Figure 8). The first region is where Σ_{line} , calculated from equations (1)-(3) assuming $f_{\text{st}} = 1$, exceeds our inferred upper limits; the second where the flux from sterile neutrinos produced at the minimal abundance from oscillations exceeds these limits. The latter provides an absolute constraint, assuming only a standard early thermal history of the universe, since the oscillations cannot be turned off.

3.1. Discussion and Conclusions

We have derived upper limits on the radiative decay of dark matter into keV photons in the ultra-faint dwarf spheroidal galaxy Willman 1, and used these to place very general

constraints on the mass and mixing angle of any sterile neutrinos that contribute to the dark matter. In doing so we adopted a total surface mass density (including Milky Way dark matter in the line of sight) of $\Sigma_{\text{dm}}(100 \text{ pc}) = 200 \text{ M}_{\odot} \text{ pc}^{-2}$ in the solid angle subtended by the *XMM-Newton* aperture corresponding to 100 pc at the Willman 1 distance of 38 kpc. While this estimate is based on equilibrium dynamical models fit to the stellar velocity dispersion profile, the dynamical status – and even the very nature of Willman 1 – were re-examined subsequent to our original X-ray observation of Willman 1 with *Chandra*. Recent optical spectroscopy supports the case that Willman 1 is (or was) a dwarf spheroidal and not a star cluster; however – in addition to the limited statistics of the velocity dispersion profile – doubts as to whether Willman 1 is in dynamical equilibrium introduce a level of uncertainty in the Willman 1 dark matter mass that must now be estimated from non-equilibrium dynamical modeling (Willman et al. 2011). Thus while our constraints are formally comparable to previous limits based on dwarf spheroidal X-ray spectroscopy (Loewenstein et al. 2009, Riemer-Sørensen & Hansen 2009, LK10, and references therein), we cannot claim to provide more stringent constraints on sterile neutrino parameters.

On the other hand we applied (for the first time) recently developed extended-source analysis methods to demonstrate the robustness and sensitivity of the *XMM-Newton* EMOS and EPN detectors to weak line emission that may arise from dark matter radiative decay – despite the fact that \sim half the data were discarded due to the effect of flares. Clearly *XMM-Newton* has an important role to play in such studies, with its larger effective area complementing the lower and more stable background of *Suzaku* and the superior spatial resolution (crucial for sources that, unlike dwarf spheroidals, have prominent intrinsic discrete source emission) of *Chandra*.

We find no confirmation of the *Chandra* evidence for an emission line at 2.5 keV (Figures 5-6). Moreover, the abundance of $m_{\text{st}} = 5 \text{ keV}$ sterile neutrinos produced by non-resonant oscillations has recently been strongly proscribed based on *Chandra* imaging spectroscopy of M31 (Watson et al. 2011), albeit in a region where baryonic matter is still prominent. Watson et al. (2011) derive an upper limit $m_{\text{st}} < 2.2 \text{ keV}$ for sterile neutrinos produced by this mechanism at the abundance required to explain all of the dark matter ($f_{\text{st}} = 1$). Combined with the lower bound from phase-space considerations of $\sim 0.3\text{-}0.4 \text{ keV}$ (Tremaine & Gunn 1979; Angus 2010), this implies that accounting for dark matter in this manner with sterile neutrinos may remain viable only at masses where the decay line lies in a spectral region dominated by blended emission features from the LHB and MWH – and, thus, sensitivity to detection at X-ray CCD spectral resolution is limited. As a result, the most significant expansion of the searchable parameter-space boundary requires, above all, the sort of leap in spectral resolution of diffuse sources possible with microcalorimeter arrays such as the Soft

X-ray Spectrometer that is part of the *Astro-H* observatory⁵ scheduled for launch in 2013. As investigation of this lower m_{st} regime proceeds, the region where off-resonant oscillations produce pulsar kicks at the high end of the observed velocity distribution (Fuller et al. 2003; Kusenko, Mandal, & Mukherjee 2008) will be probed.

Alternatively, the sterile neutrino abundance may be subdominant ($f_{\text{st}} < 1$), or accounted for by means in addition to the DW production mechanism. The production of sterile neutrinos via oscillations may be resonantly enhanced in the presence of nonzero lepton asymmetry (Shi & Fuller 1999; Kishimoto, Fuller, & Smith 2006; Laine & Shaposhnikov 2008), thus opening up a larger region in the $m_{\text{st}} - \theta$ plane consistent with observed line emission constraints and $f_{\text{st}} = 1$. Other suggested production mechanisms, i.e. from inflaton or Higgs decay, do not involve oscillations and are therefore independent of the mixing angle (Kusenko 2006; Shaposhnikov & Tkachev 2006; Petraki & Kusenko 2008). Furthermore, if sterile neutrinos are produced above the electroweak scale (Kusenko 2006; Petraki & Kusenko 2008; Kusenko, Takahashi, & Yanagida 2010), or if some other sterile neutrinos decay and produce entropy (Asaka et al. 2006; Fuller et al. 2009, 2011), both the abundance and the clustering properties of dark matter are affected. However should the pulsar kick and non-resonant oscillation domains be ruled out, the expected detectability of sterile neutrino radiative decay lines becomes essentially undetermined.

Despite ongoing dedicated production and direct detection experiments, as well as intensive indirect searches, successful discovery of CDM in the form of weakly interacting massive particles (WIMPs) remains elusive. Given the prevalence of sterile neutrinos in extensions of the standard model that explain the generation of neutrino masses, the emergence of the keV scale as a natural one for some recently proposed production scenarios (Kusenko, Takahashi, & Yanagida 2010; Merle 2012), and indications that cosmogonies dominated by WDM may explain discrepancies between CDM and observations of small-scale structure and galaxy formation (Lovell et al. 2011; Menci, Fiore, & Lamastra 2012; Yue & Chen 2012), strong physical motivation for their search persists. In addition, there are other decaying keV dark matter candidates, one of which – moduli dark matter – we are currently investigating (Loewenstein, Kusenko, & Yanagida 2012).

We thank Steve Snowden and Dave Davis for their advice on *XMM-Newton* data analysis issues, and Beth Willman for comments on the draft manuscript and input on observing and funding proposals. This work was supported by NASA ADAP Grant #NNX11AD36G. AK acknowledges additional support from DOE Grant #DE-FG03-91ER40662.

⁵<http://heasarc.gsfc.nasa.gov/docs/astroh/>

This work is based on observations obtained with *XMM-Newton*, an ESA science mission with instruments and contributions directly funded by ESA Member States and the USA (NASA), and utilized software integrated and maintained at the *XMM-Newton* Science Operations Center. Additionally, use was made of data and/or software provided by the High Energy Astrophysics Science Archive Research Center (HEASARC), which is a service of the Astrophysics Science Division at NASA/GSFC and the High Energy Astrophysics Division of the Smithsonian Astrophysical Observatory. Finally, use was made of NASA's Astrophysics Data System, and the arXiv e-print service operated by Cornell University.

REFERENCES

- Abazajian, K., Fuller, G. M., & Patel, M. 2001, *Phys. Rev. D*, 64, 023501
- Abazajian, K., Fuller, G. M., & Tucker, W. H. 2001, *ApJ*, 562, 593
- Amorisco, N. C., & Evans, N. W. 2011, *MNRAS*, 411, 2118
- Ando, S., & Kusenko, A. 2010, *Phys. Rev. D*, 81, 113006
- Angus, G. 2010, *J. Cosmology Astropart. Phys.*, 3, 26
- Asaka, T., Shaposhnikov, M., & Laine, M. 2007, *JHEP*, 01, 091
- Asaka, T., & Shaposhnikov, M. 2005, *Physics Letters B*, 620, 17
- Asaka, T., Shaposhnikov, M., & Kusenko, A. 2006, *Physics Letters B*, 638, 401
- Asplund M., Grevesse N., Sauval A.J. & Scott P. 2009, *ARA&A*, 47, 481
- Baldi, A., Etti, S., Molendi, S., Balestra, I., Gastaldello, F., & Tozzi, P. 2012, *A&A*, 537, 142
- Bezrukov, F., & Shaposhnikov, M. 2007, *Phys. Rev. D*, 75, 053005
- Boyanovsky, D. 2008, *Phys. Rev. D*, 78, 103505
- Boyanovsky, D., & Wu, J. 2011, *Phys. Rev. D*, 83, 043524
- Boyarsky, A., Ruchayskiy, O., & Shaposhnikov, M. 2009, *Annual Review of Nuclear and Particle Science*, 59, 191
- Cash, W. 1979, *ApJ*, 228, 939

- Dickey, J., & Lockman, F. J. 1990, ARA&A, 28, 21
- Dodelson, S., & Widrow, L. M. 1994, Phys. Rev. Lett., 72, 17
- Dunstan, R. M., Abazajian, K. N., Polisensky, E., & Ricotti, M. 2011, Phys. Rev. D, submitted (arXiv:1109.6291)
- Ferrero, I., Abadi, M. G., Navarro, J. F., Sales, L. V., & Gurovich, S. 2011, MNRAS, submitted (arXiv:1111.6609)
- Fukugita, M. & Yanagida, T. T., Phys. Lett. B **174**, 45 (1986).
- Fuller, G. M., Kishimoto, C. T., & Kusenko, A. 2011, arXiv:1110.6479
- Fuller, G. M., Kusenko, A., Mocioiu, I., & Pascoli, S. 2003, Phys. Rev. D, 68, 103002
- Fuller, G. M., Kusenko, A., & Petraki, K. 2009, Physics Letters B, 670, 281
- Kishimoto C. T., Fuller G. M., & Smith C. J. 2006, Phys. Rev. Lett., 97, 141301
- Kuntz, K. D., & Snowden, S. L. 2008, A&A, 478, 575
- Kusenko, A. 2006, Physical Review Letters, 97, 241301
- Kusenko, A. 2009, Phys. Rept., 481, 1
- Kusenko, A., Mandal, B. P., & Mukherjee, A. 2008, Phys. Rev. D, 77, 123009
- Kusenko, A., & Segrè, G. 1997, Physics Letters B, 396, 197
- Kusenko, A., Takahashi, F., & Yanagida, T. T. 2010, Phys. Lett. B, 693, 144
- Kushino, A., Ishisaki, Y., Morita, U., Yamasaki, N. Y., Ishida, M., Ohashi, T., & Ueda, Y. 2002, PASJ, 54,327
- Laine M., & Shaposhnikov, M. 2008, J. Cosmology Astropart. Phys., 6, 031
- Loewenstein, M., & Kusenko, A. 2010, ApJ, 714, 652 (LK10)
- Loewenstein, M., Kusenko, A., & Biermann, P. L. 2009, ApJ, 700, 426
- Loewenstein, M., Kusenko, A., & Yanagida, T. T. 2012, in preparation
- Lovell, M., Eke, V., Frenk, C., Gao, L., Jenkins, A., Theuns, T., Wang, J., Boyarsky, A., & Ruchayskiy, O. 2011, MNRAS, in press (arXiv:1104.2929)

- Menci, N., Fiore, F., & Lamastra, A. 2012, MNRAS, in press (arXiv:1201.1617)
- Merle, A., 2012, in Proceedings for the TAUP 2011 conference, Munich, Germany, in press (arXiv:1201.0881)
- Navarro J. F., Frenk C. S., & White S. D. M. 1997, ApJ, 490, 493
- Nevalainen, J., Markevitch, M., & Lumb, D. 2005, ApJ, 629, 172
- Oguri, M., & Hamana, T. 2011, MNRAS, 414, 1851
- Petraki, K. 2008, Phys. Rev. D, 77, 105004
- Petraki, K., & Kusenko, A. 2008, Phys. Rev. D, 77, 065014
- Riemer-Sørensen, S.; Hansen, S. H. 2009, A&A, 500, L37
- Sánchez-Conde, M. A., Cannoni, M., Zandanel, F., Gómez, M. E., & Prada, F. 2011, J. Cosmology Astropart. Phys., 12, 011
- Shaposhnikov, M., & Tkachev, I. 2006, Physics Letters B, 639, 414
- Shi, X., & Fuller, G. M. 1999, Phys. Rev. Lett., 82, 2832
- Snowden, S. L., Mushotzky, R. F., Kuntz, K. D., & Davis, D. S. 2008, A&A, 478, 615
- Strigari, L. E., Koushiappas, S. M., Bullock, J. S., Kaplinghat, M., Simon, J. D., Geha, M., & Willman, B. 2008, ApJ, 678, 614
- Tremaine, S., & Gunn, J. E. 1979, Phys. Rev. Lett., 42, 407
- Watson, C. R., Li, Z., & Polley, N. K., J. Cosmology Astropart. Phys., in press (arXiv:1111.4217)
- Willman, B., Geha, M., Strader, J., Strigari, L. E., Simon, J. D., Kirby, E., Ho, N., Warres, A. 2011, AJ, 142, 128
- Wilms, J., Allen, A., & McCray, R. 2000, ApJ, 542, 941
- Wolf, J., Martinez, G. D., Bullock, J. S., Kaplinghat, M., Geha, M., Munoz, R. R., Simon, J. D., & Avedo, F. F. 2009, MNRAS, 406, 122
- Yue, B., & Chen, X. 2012, ApJ, in press (arXiv:1201.3686)

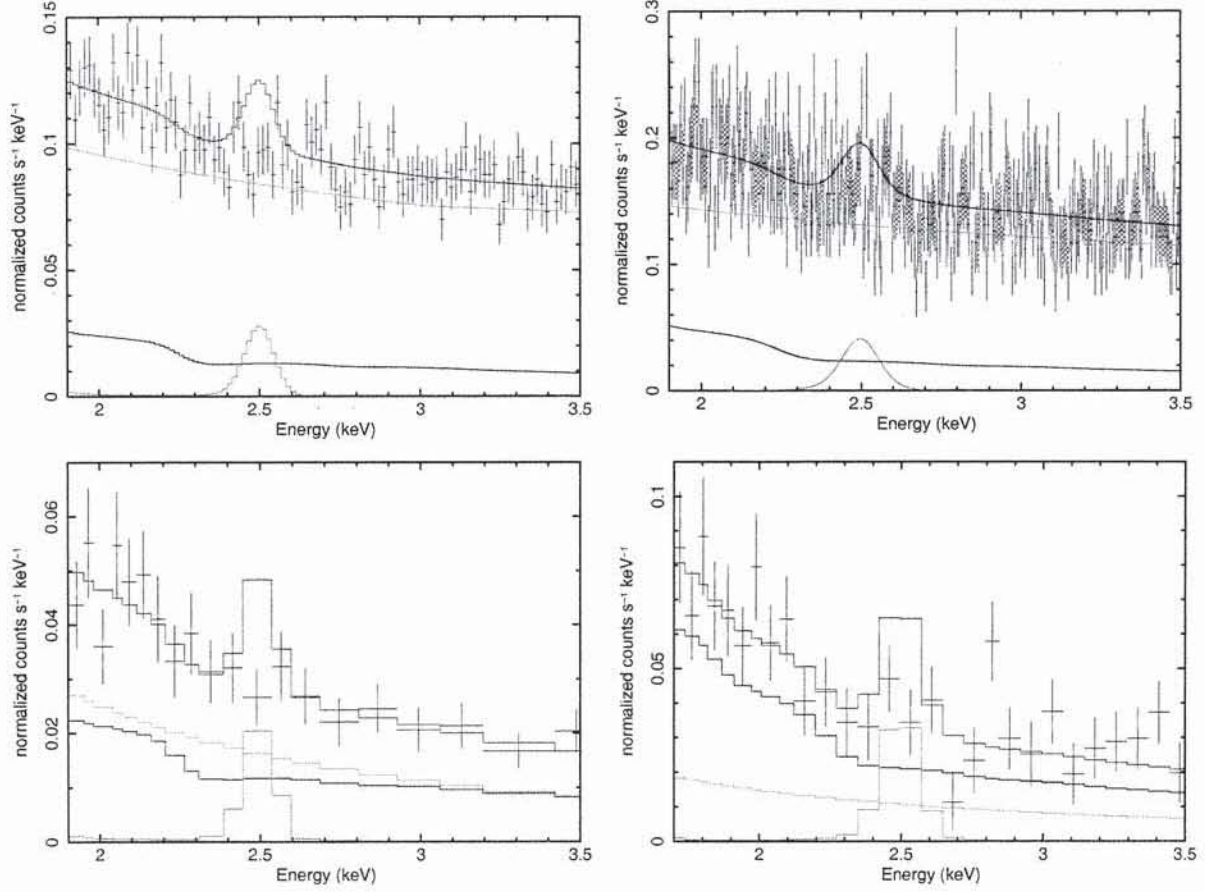


Fig. 6.— Unbinned EMOS (*upper left panel (a)*) and EPN (*upper right panel (b)*), and binned EMOS (*lower left panel (c)*) and EPN (*lower right panel (d)*) spectra (black errorbars) with best-fit models (and their decomposition) that include a narrow 2.5 keV emission line with strength fixed at that predicted for radiative decay of sterile neutrinos produced by non-resonant oscillations (see Figure 5). The upper and lower curves correspond to the *cstat-nbs* and χ^2 -*bs* approaches, respectively. The color coding follows Figure 1, with the additional line component in orange.

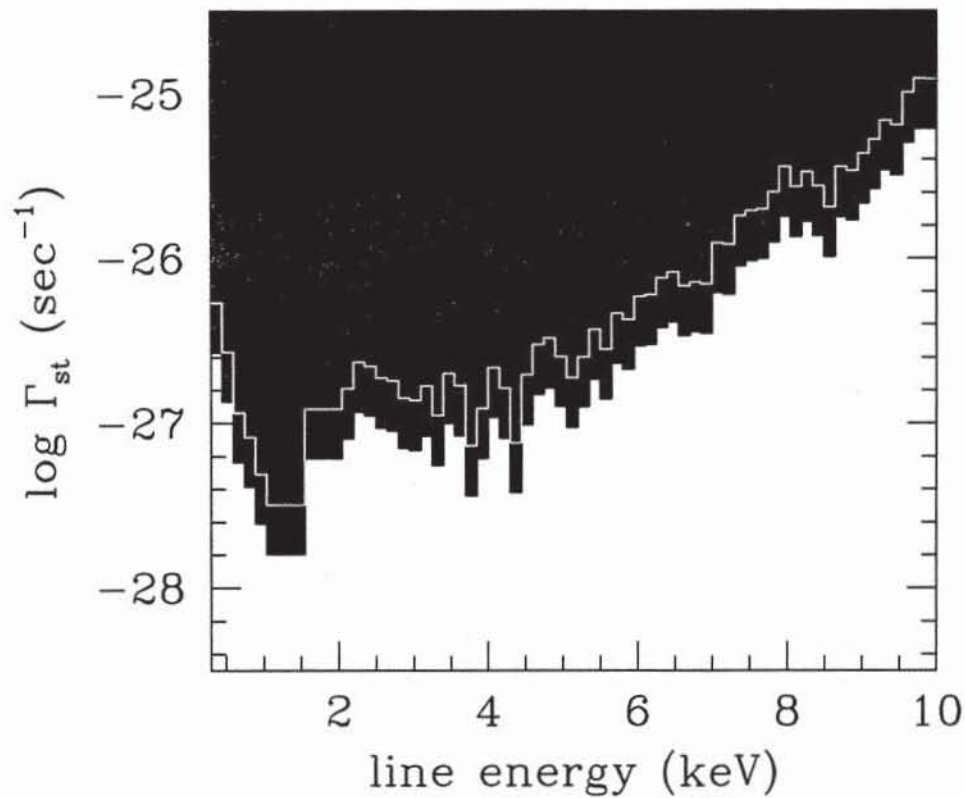


Fig. 7.— Excluded dark matter radiative decay rates (filled region) as a function of line energy derived from the upper limit on the average emission line surface brightness emerging from the inner 100 pc of Willman 1, assuming $\Sigma_{dm}(100 \text{ pc}) = 200 \text{ M}_{\odot} \text{ pc}^{-2}$ of decaying dark matter. The yellow histogram shows the corresponding limits for $\Sigma_{dm}(100 \text{ pc}) = 100 \text{ M}_{\odot} \text{ pc}^{-2}$ – most of which would originate in the Milky Way halo.

